Journal of the Mechanics and Physics of Solids 133 (2019) 103729

Contents lists available at ScienceDirect

Journal of the Mechanics and Physics of Solids

journal homepage: www.elsevier.com/locate/jmps

A thermo-mechanically coupled finite strain model for phase-transitioning austenitic steels in ambient to cryogenic temperature range

Mrityunjay Kothari, Sijun Niu, Vikas Srivastava*

School of Engineering, Brown University, Providence RI 02912, United States

ARTICLE INFO

Article history:
Received 11 July 2019
Revised 8 September 2019
Accepted 13 September 2019
Available online 14 September 2019

Keywords:
Austenite
Cryogenic temperature
Strain induced martensite
Phase transition
316L stainless steel
Finite strain
Thermo-mechanical model
LNG

ABSTRACT

We present a finite-strain thermo-mechanically coupled continuum theory to model the material response of phase transitioning (metastable) austenitic steels from ambient (room) to cryogenic temperature. We applied our model to 316L stainless steel which shows plastic strain driven transformation from FCC austenite to BCC martensite phase at temperatures below room temperature and calibrated the model parameters using uniaxial tension tests at room and cryogenic temperatures. The constitutive model is able to successfully model the observed second strain-hardening behavior at cryogenic temperature due to formation of harder martensite at large strains. We implemented our coupled thermo-mechanical-phase transition model in the finite element program Abaqus by writing a user material subroutine and validated the model by conducting finite element based tension and compression simulations for a room temperature formed corrugated pipe. Comparisons of mechanical response between our simulation predictions and full-scale tests for the corrugated pipe at both room and cryogenic temperature show good accuracy of our model. We also conducted simulations to investigate the austenite-martensite phase transition near a notch tip in a flat plate geometry.

1. Introduction

Austenitic steels are widely used in the industry for their excellent ductility, strength and corrosion resistance over a wide range of temperatures. Automotive industries (Bleck and Schael, 2000; Jacques et al., 2007) and cryogenic applications (e.g. Liquefied Natural Gas (LNG) flexible pipes) (Choi et al., 2012a; 2012b; Chul Kim et al., 2011; Kim et al., 2014; 2012; 2013; Ryoo et al., 2011; Srivastava et al., 2011; Tyshchenko et al., 2010; Yang et al., 2017) are some examples where phase transitioning austenitic steels play an important role. In the LNG transport pipes, steels used for cryogenic LNG containment layer experience complex thermo-mechanical loading history in which they are plastically formed at room temperature during the cold forming process and are subjected to operating loads at cryogenic temperature (loads on LNG transfer pipes in an offshore environment can be very severe). The steels for LNG applications such as 316L stainless steels (SS) are austenitic steels that exhibit history-dependent, plastic strain driven austenite-martensite transformation that allows substantial strain-hardening.

* Corresponding author.
E-mail address: vikas_srivastava@brown.edu (V. Srivastava).

https://doi.org/10.1016/j.jmps.2019.103729
0022-5096/

At cryogenic temperatures, austenitic steels show a prominent temperature-driven austenite-martensite transformation. If austenite is cooled below a certain temperature known as *martensite start temperature* (M_s), it spontaneously transforms into martensite. The martensite volume fraction evolves very rapidly in time and is governed by Koistinen-Marburger equation (Koistinen and Marburger, 1959). Deep cryogenic treatment is sometimes performed in certain types of steels to obtain low-temperature martensitic transformation for tool steels with excellent wear properties (Gavriljuk et al., 2013; Tyshchenko et al., 2010). For 300-series austenitic steels, the values of M_s are below $0\,K$, making these steels stable to *purely temperature-driven* spontaneous martensitic phase transformation. However, these steels are *metastable* since they can undergo *plasticity-driven phase transformation to martensite* for temperatures above M_s. The plasticity-driven phase transformation kinetics are strongly temperature dependent. While at room temperature, no substantial amount of martensite forms even for large plastic strains, the kinetics change rapidly at lower temperatures. At cryogenic temperatures, austenitic phase can rapidly transform into martensitic phase through a strain-assisted mechanism (Olson and Cohen, 1975). The volume fraction of martensite depends on the temperature, deformation history, and alloy composition. Since the α'-martensite offers much higher resistance to plastic flow than the γ- austenite, as the SS is deformed, a *second strain-hardening* is often observed.

In this paper, we model the response of metastable austenitic steels and their transformation to martensite in the room to cryogenic temperature range. Metastability increases the formability of the steel and makes austenitic steels especially attractive for automobile parts (Bleck and Schael, 2000; Jacques et al., 2007; Kim et al., 2004) and pipes for cryogenic applications like LNG transport (Choi et al., 2012a; 2012b; Chul Kim et al., 2011; Kim et al., 2014; 2012; 2013; Ryoo et al., 2011; Yang et al., 2017). The austenitic γ phase is face-centered cubic (FCC) which transforms into hexagonal closed packed (HCP)ε-martensite and body-centered cubic (BCC) α'-martensite. ANGEL and T. (1954) studied the austenite-martensite transformation in 304 SS and proposed an empirical relation for the evolution of martensite volume fraction. Olson and Cohen identified the intersection of shear-bands as a nucleation mechanism for martensite embryos and developed a physically-motivated model for evolution of martensite volume fraction in plastically deformed austenitic steels (Levitas et al., 1998; Olson and Cohen, 1975). Narutani et al. (1982) proposed a constitutive relation to predict the flow behavior of transforming metastable austenitic steels based on transformation kinetics and flow properties of individual phases. The authors identified static-hardening and dynamic-softening effects arising from martensitic transformation as the two major factors controlling the flow stress. Stringfellow et al. (1992) developed a constitutive model for transforming metastable austenitic steels where the transformation kinetics were modeled to be dependent on plastic strain, temperature and stress state. Diani and Parks (1998) modeled the martensite evolution in TRIP (Transformation Induced Plasticity) steels undergoing a multiaxial thermomechanical loading by focusing on deformation mechanisms within the grain and studied austenitic steels with low stacking fault energy. Levitas et al. (1998) developed a continuum thermo-mechanical model for martensitic phase transformation in TRIP steels and presented a numerical solution of shear-band intersection based martensitic phase transformation. The model was based on multiplicative decomposition of the total deformation gradient into elastic, plastic and transformation parts, and generalized Prandtl-Reuss equations (Levitas, 1997a; 1997b; 1998). Garion and Skoczen (2002) developed a small-strain, homogenization-based constitutive model for austenite-martensite transformation in 316L steel at cryogenic temperatures. They approximated the evolution of martensite volume fraction in 316L by a linearized form. More recently, Lee et al. (2009) proposed a Bodner-type damage model to explain the discontinuous yielding phenomenon in austenitic steels at low temperatures.

While several additional meaningful contributions have been made through recent experimental (Celada-Casero et al., 2017; Lee et al., 2019a; 2019b; Talonen and Hanninen, 2007; Wang and Beese, 2019) and modeling work (Hamasaki et al., 2018; Mansourinejad and Ketabchi, 2017; Zaera et al., 2012; Zecevic et al., 2019) on austenite-martensite transformation in steels, there are significant modeling gaps and needs, especially for the cryogenic temperature applications. Most of the work till date on modeling austenitic steels in the cryogenic temperature range is limited to small strains and small martensite volume fractions, and often employ linear approximations to the sigmoidal evolution form proposed in Olson and Cohen (1975). Additionally, these models are limited to isothermal deformation and a three-dimensional (3D) theoretical large strain model that can seamlessly predict thermo-mechanical-phase transition response is lacking. In applications, SS is often exposed to a combination of thermo-mechanical loading conditions; an example is cold working of steels to form their shapes and subsequent *in-service* deformation at differing cold temperatures. Austenitic phase transitioning SS are employed in many cryogenic applications and at such temperatures, *pre-strains* can cause significant differences in austenite-martensite volume fractions as well as in stress-strain response of the steel. Due to the temperature and plastic strain dependence of phase transformation (increasing martensite volume fraction), the strain-hardening response of SS for heterogeneously strained structures is quite complex and difficult to predict experimentally. To address these challenges, we present a 3D, finite strain, thermo-mechanically coupled continuum theory for phase transitioning austenitic steels to model their isotropic response under complex thermo-mechanical loading for a temperature range that spans room temperature to cryogenic temperature. We have calibrated the model parameters for 316L SS by using tension tests conducted in Buitrago et al. (2010); Srivastava et al. (2011). We implemented our model in the finite element program Abqaus Standard by writing a user material subroutine UMAT. The model is validated by simulating a full-scale corrugated flexible pipe geometry commonly used for LNG transport and comparing it with experiments in Srivastava et al. (2011). Further, we applied our model to evaluate a simple notch-test geometry and show the effects of phase transition on the global and local structural response.

The plan of this paper is as follows. In Section 2 we develop a physically motivated continuum thermo-mechanical model and obtain the model parameters for 316L SS. In Section 3, we predict and discuss some typical uniaxial temperature deformation history cases using our model. In Section 4 we validate the predictive capabilities of our model by comparing finite

element simulation results against tension and compression tests (involving local inhomogeneous deformations) conducted on a full-scale corrugated LNG pipe. In Section 5, we discuss martensite evolution and its effect on local and global response in presence of a notch. We summarize our findings and conclude the paper in Section 6.

2. Thermo-mechanical theoretical framework

In this section we develop a coupled thermo-mechanical framework for modeling of metastable austenitic steel.

2.1. Kinematics

We adopt a finite strain framework[1] and assume Kröner-Lee multiplicative decomposition (Lee, 1969) of the deformation gradient $\mathbf{F}(\mathbf{x})$ into elastic and plastic parts $\mathbf{F}^e$ and $\mathbf{F}^p$ as

$$\mathbf{F} = \mathbf{F}^e\mathbf{F}^p, \qquad \text{with} \qquad \det\mathbf{F}^e > 0 \quad \text{and} \quad \det\mathbf{F}^p > 0, \tag{2.1}$$

where $\mathbf{x}$ represents the material point in the reference configuration. The velocity gradient is related to the deformation gradient $\mathbf{F}$ through

$$\mathbf{L} = \dot{\mathbf{F}}\mathbf{F}^{-1}. \tag{2.2}$$

Velocity gradient $\mathbf{L}$ can be decomposed into elastic and plastic distortion-rate tensors $\mathbf{L}^e$ and $\mathbf{L}^p$ as,

$$\mathbf{L}^e = \dot{\mathbf{F}}^e\mathbf{F}^{e-1} \quad \text{and} \quad \mathbf{L}^p = \dot{\mathbf{F}}^p\mathbf{F}^{p-1}. \tag{2.3}$$

Symmetric part of $\mathbf{L}^e$ is defined as elastic stretching $\mathbf{D}^e$ and symmetric part of $\mathbf{L}^p$ is defined as plastic stretching $\mathbf{D}^p$.

$$\mathbf{D}^e = \frac{1}{2}(\mathbf{L}^e + \mathbf{L}^{e^\top}) \tag{2.4}$$

$$\mathbf{D}^p = \frac{1}{2}(\mathbf{L}^p + \mathbf{L}^{p^\top}) \tag{2.5}$$

We make the standard assumption that plastic flow is incompressible and hence $\det\mathbf{F}^p = 1$ and $\mathrm{tr}\,\mathbf{D}^p = 0$. Green strain is defined as,

$$\mathbf{E}^e = \frac{1}{2}(\mathbf{C}^e - \mathbf{1}) \quad \text{and} \quad \mathbf{C}^e = \mathbf{F}^{e\top}\mathbf{F}^e. \tag{2.6}$$

2.2. Constitutive equations

1. **Free energy:** To represent the macro scale mechanical response of a material point consisting of austenite and martensite phases, we adopt a Voigt composite formulation. We assume that the constitutive response of the austenite-martensite steel is such that both phases experience the same deformation gradient.[2] The Kröner-Lee decomposition for the two phases gives,

$$\mathbf{F} = \mathbf{F}^e_\gamma\mathbf{F}^p_\gamma = \mathbf{F}^e_{\alpha'}\mathbf{F}^p_{\alpha'}. \tag{2.7}$$

We assume that the free energy density ψ (measured per unit reference volume) can be decomposed as

$$\psi = \phi_\gamma\,\psi_\gamma(\mathbf{C}^e_\gamma, \vartheta) + \phi_{\alpha'}\,\psi_{\alpha'}(\mathbf{C}^e_{\alpha'}, \vartheta) \quad \text{and} \quad \phi_\gamma + \phi_{\alpha'} = 1, \tag{2.8}$$

where, for the austenite phase,

$$\psi_\gamma = G_\gamma|\mathbf{E}^e_\gamma|^2 + \frac{\lambda_\gamma}{2}(\mathrm{tr}\,\mathbf{E}^e_\gamma)^2 - \alpha^{\mathrm{th}}_\gamma(2G_\gamma + 3\lambda_\gamma)(\vartheta - \vartheta_0)\mathrm{tr}\,\mathbf{E}^e_\gamma - \frac{C_\gamma}{2\vartheta_0}(\vartheta - \vartheta_0)^2 \tag{2.9}$$

$$\mathbf{E}^e_\gamma = \frac{1}{2}(\mathbf{C}^e_\gamma - \mathbf{1}) \quad \text{and} \quad \mathbf{C}^e_\gamma = \mathbf{F}^{e\top}_\gamma\mathbf{F}^e_\gamma \tag{2.10}$$

and similarly for the martensite phase,

$$\psi_{\alpha'} = G_{\alpha'}|\mathbf{E}^e_{\alpha'}|^2 + \frac{\lambda_{\alpha'}}{2}(\mathrm{tr}\,\mathbf{E}^e_{\alpha'})^2 - \alpha^{\mathrm{th}}_{\alpha'}(2G_{\alpha'} + 3\lambda_{\alpha'})(\vartheta - \vartheta_0)\mathrm{tr}\,\mathbf{E}^e_{\alpha'} - \frac{C_{\alpha'}}{2\vartheta_0}(\vartheta - \vartheta_0)^2 \tag{2.11}$$

[1] Notation: We use standard notation of continuum mechanics. Specifically: Bold capital letters represent second order tensor; a superposed dot denotes the material time-derivative; $\mathrm{tr}\mathbf{A}$, $\det\mathbf{A}$, and $|\mathbf{A}| = \sqrt{\mathbf{A}:\mathbf{A}}$ represent trace, determinant and magnitude of a tensor $\mathbf{A}$.

[2] A similar form for steel was discussed in Narutani et al. (1982). A homogenization-based approach wherein α' platelets embedded in the γ−austenite matrix are treated as Eshelby inclusions is another method/assumption to model the response of austenite-martensite steel (Garion et al., 2006; Iwamoto, 2004; Stringfellow et al., 1992). We find that a Voigt-like mathematical framework is a good approximation under finite strains, considering the martensitic transformation becomes significant only at larger strains.

$$\mathbf{E}^e_{\alpha'} = \frac{1}{2}(\mathbf{C}^e_{\alpha'} - \mathbf{1}) \quad \text{and} \quad \mathbf{C}^e_{\alpha'} = \mathbf{F}^{e^\top}_{\alpha'}\mathbf{F}^e_{\alpha'}. \tag{2.12}$$

Here λ, G denote the shear modulus and Lame constant respectively, α^{th} denotes the coefficient of thermal expansion and C denotes the heat capacity. The subscripts γ and α' denote austenite and martensite phases respectively and ϕ denotes their volume fractions.

2. **Stress:**
The driving stress for plastic flow is the *symmetric* Mandel stress. From the above development, the Mandel stress in the two phases can be written as,

$$\mathbf{M}^e_\gamma = \frac{\partial \psi_\gamma}{\partial \mathbf{E}^e_\gamma} = 2G_\gamma \mathbf{E}^e_\gamma + \lambda_\gamma (\text{tr}\,\mathbf{E}^e_\gamma)\mathbf{1} - \alpha^{\text{th}}_\gamma (2G_\gamma + 3\lambda_\gamma)(\vartheta - \vartheta_0)\mathbf{1} \tag{2.13}$$

$$\mathbf{M}^e_{\alpha'} = \frac{\partial \psi_{\alpha'}}{\partial \mathbf{E}^e_{\alpha'}} = 2G_{\alpha'} \mathbf{E}^e_{\alpha'} + \lambda_{\alpha'} (\text{tr}\,\mathbf{E}^e_{\alpha'})\mathbf{1} - \alpha^{\text{th}}_{\alpha'} (2G_{\alpha'} + 3\lambda_{\alpha'})(\vartheta - \vartheta_0)\mathbf{1}. \tag{2.14}$$

We make the following simplifying assumptions,

$$G_\gamma \approx G_{\alpha'} = G, \tag{2.15}$$

$$\lambda_\gamma \approx \lambda_{\alpha'} = \lambda, \tag{2.16}$$

$$\alpha^{\text{th}}_\gamma \approx \alpha^{\text{th}}_{\alpha'} = \alpha_{\text{th}}. \tag{2.17}$$

Note $\lambda = \frac{2G\nu}{1-2\nu}$, where ν is the Poisson's ratio.
The Mandel stress for the two phases can then be written as,

$$\mathbf{M}^e_\gamma = 2G\mathbf{E}^e_\gamma + \lambda(\text{tr}\,\mathbf{E}^e_\gamma)\mathbf{1} - \alpha_{\text{th}}(2G + 3\lambda)(\vartheta - \vartheta_0)\mathbf{1} \tag{2.18}$$

$$\mathbf{M}^e_{\alpha'} = 2G\mathbf{E}^e_{\alpha'} + \lambda(\text{tr}\,\mathbf{E}^e_{\alpha'})\mathbf{1} - \alpha_{\text{th}}(2G + 3\lambda)(\vartheta - \vartheta_0)\mathbf{1}. \tag{2.19}$$

For a two-phase Voigt composite,[3] the total Mandel stress, $\mathbf{M}$, is

$$\mathbf{M}^e = \phi_\gamma \mathbf{M}^e_\gamma + \phi_{\alpha'} \mathbf{M}^e_{\alpha'} \tag{2.20}$$

and the total Cauchy stress, $\mathbf{T}$ is,

$$\mathbf{T} = \phi_\gamma \mathbf{T}_\gamma + \phi_{\alpha'} \mathbf{T}_{\alpha'}, \tag{2.21}$$

where the individual contributions to total Cauchy stress from austenite and martensite phases are $\phi_\gamma \mathbf{T}_\gamma$ and $\phi_{\alpha'}\mathbf{T}_{\alpha'}$, respectively. We also have the following relation

$$\mathbf{T}_\gamma = J^{-1}\mathbf{F}^e_\gamma \mathbf{M}^e_\gamma \mathbf{F}^{e^\top}_\gamma \tag{2.22}$$

$$\mathbf{T}_{\alpha'} = J^{-1}\mathbf{F}^e_{\alpha'} \mathbf{M}^e_{\alpha'} \mathbf{F}^{e^\top}_{\alpha'} \tag{2.23}$$

with $J = \det \mathbf{F}$.

3. **Flow rule:**
We adopt the Mises Flow Rule for both the phases as

$$\bar{\sigma}_\gamma \equiv \sqrt{\frac{3}{2}}\,|\mathbf{M}^e_{0\gamma}| = Y_\gamma(\bar{\varepsilon}_{p\gamma}) \quad \text{for} \quad \mathbf{D}^p_\gamma \neq \mathbf{0} \tag{2.24}$$

$$\sqrt{\frac{3}{2}}\,\dot{\bar{\varepsilon}}_{p\gamma} = |\mathbf{D}^p_\gamma|, \quad \bar{\varepsilon}_{p\gamma}(\mathbf{X}, 0) = 0 \tag{2.25}$$

where $\bar{\sigma}_\gamma$ is the *equivalent von Mises stress*, $\dot{\bar{\varepsilon}}_{p\gamma}$ is the *equivalent tensile plastic strain rate* and $\bar{\varepsilon}_{p\gamma}$ is the *accumulated plastic strain* for the austenite phase. We assume that the direction of the deviatoric stress $\mathbf{M}^e_{0\gamma}$ and the direction of

[3] We are primarily interested in large strain response when we consider the two phase system response (martensite formation at very small strains is negligible). At large strains, a reasonable approximation is

$$\mathbf{E}^e_\gamma \approx \mathbf{E}^e_{\alpha'} \approx \mathbf{E}^e$$

plastic stretching $\mathbf{N}^p_\gamma$ coincide, also known as the *codirectionality hypothesis*, therefore

$$\sqrt{\frac{3}{2}}\mathbf{M}^e_{0\gamma} = Y_\gamma(\bar{\varepsilon}_{p\gamma})\mathbf{N}^p_\gamma. \tag{2.26}$$

We introduce a yield function,

$$f_\gamma = \sqrt{\frac{3}{2}}\,|\mathbf{M}^e_{0\gamma}| - Y_\gamma(\bar{\varepsilon}_{p\gamma}), \tag{2.27}$$

define a no-flow condition as

$$\mathbf{D}^p_\gamma = 0 \quad \text{if} \quad f_\gamma < 0 \quad \text{or if} \quad f_\gamma = 0 \quad \text{and} \quad \dot{f}_\gamma < 0, \tag{2.28}$$

and the consistency condition as

$$\text{if} \quad \mathbf{D}^p_\gamma \neq 0 \quad \text{then} \quad f_\gamma = 0 \quad \text{and} \quad \dot{f}_\gamma = 0. \tag{2.29}$$

The flow rule for martensite is obtained similarly. For our two-phase composite, the total deviatoric Mandel stress follows from Eqs. (2.21) and (2.26) as

$$\sqrt{\frac{3}{2}}\mathbf{M}^e_0 = \phi_\gamma Y_\gamma(\bar{\varepsilon}_{p\gamma})\mathbf{N}^p_\gamma + \phi_{\alpha'} Y_{\alpha'}(\bar{\varepsilon}_{p\alpha'})\mathbf{N}^p_{\alpha'} \tag{2.30}$$

Assuming that the plastic flow in austenite and martensite are codirectional,

$$\mathbf{N}^p_\gamma \approx \mathbf{N}^p_{\alpha'} = \mathbf{N}^p. \tag{2.31}$$

The *total deviatoric Mandel stress for the austenite-martensite (composite) material point* is given as,

$$\sqrt{\frac{3}{2}}\mathbf{M}^e_0 = \{\phi_\gamma Y_\gamma(\bar{\varepsilon}_{p\gamma}) + \phi_{\alpha'} Y_{\alpha'}(\bar{\varepsilon}_{p\alpha'})\}\mathbf{N}^p. \tag{2.32}$$

Further, Narutani et al. (1982) used experimental evidence from forming operations to explain that transformed martensite inherits the same substructure as the deformed austenite. Also, significant martensite volume fraction forms only above moderate plastic strains. For these large strains, we can assume that the elastic strains are negligible compared to the total strains. Following Narutani et al.'s study indicating equivalent deformation and assuming elastic strains negligible compared to the total strain, gives us

$$\bar{\varepsilon}_{p\gamma} \approx \bar{\varepsilon}_{p\alpha'} \approx \bar{\varepsilon}_p. \tag{2.33}$$

Therefore, the combined yield function for the austenite-martensite composite is given as,

$$Y(\bar{\varepsilon}_p) = \phi_\gamma Y_\gamma(\bar{\varepsilon}_p) + \phi_{\alpha'} Y_{\alpha'}(\bar{\varepsilon}_p). \tag{2.34}$$

4. **Equations for heat flux and temperature evolution:**
We assume the heat flux to be governed by the Fourier's law

$$\mathbf{q} = -\kappa\nabla\vartheta, \tag{2.35}$$

where $\mathbf{q}$ is the heat flux defined in the reference frame and κ is the thermal conductivity with the assumption $\kappa_\gamma \approx \kappa_{\alpha'} = \kappa$.
Balance of energy for the two phase system gives us (Srivastava et al., 2010a; 2010b),

$$\rho C\,\dot{\vartheta} = -\mathrm{Div}\,\mathbf{q} + \omega(\phi_\gamma\bar{\sigma}_\gamma\dot{\bar{\varepsilon}}_{p\gamma} + \phi_{\alpha'}\bar{\sigma}_{\alpha'}\dot{\bar{\varepsilon}}_{p\alpha'}) - \rho\, l\,\dot{\phi}_{\alpha'} \tag{2.36}$$

where, C is the effective specific heat for the two-phase steel with $C_\gamma \approx C_{\alpha'} = C$. $\omega \sim 0.9$ is the fraction of the plastic work that is converted to heat (Brown et al., 1989), $\rho = 7800\,\mathrm{kg/m^3}$ is the equivalent density of steel, and l is the latent heat due to martensitic phase transformation (Tomita and Iwamoto, 1995).

5. **Isotropic hardening law for austenite-martensite steel:**
In the following, we develop the isotropic hardening law from physically motivated mechanisms for a single phase steel. The same physical mechanisms apply to both the γ and α' phases so we will generalize the hardening law to two-phase steels.
The resistance to initial macroscopic plastic deformation is characterized by yield strength. The temperature dependence of yield strength originates from thermally activated motion of dislocations under the action of applied forces. The resistance to dislocation motion can be decomposed into two components (Conrad, 1964; 1970; Conrad and Wiedersich, 1960; Kocks and Mecking, 2003; Seeger, 1955):

$$\bar{\sigma}_{Y\gamma} = \bar{\sigma}_{A\gamma} + \bar{\sigma}_{T\gamma} \tag{2.37}$$

Here $\bar{\sigma}_{A\gamma}$ is the athermal component arising due to long-range stresses and it is temperature independent. $\bar{\sigma}_{T\gamma}$, on the other hand, arises from short-range obstacles to the motion of dislocations and is temperature dependent. For temperatures $\geq 0.25\vartheta_m$ where ϑ_m is the melting temperature of the steel, the thermal component of resistance becomes negligible

and only athermal component remains. Following Reed and Horiuchi (2011), for the temperature range considered in this paper, we choose a phenomenological form for the thermal component as

$$\bar{\sigma}_{T\gamma} = (\bar{\sigma}_{0\gamma} - \bar{\sigma}_{A\gamma}) \exp(-c_\gamma \vartheta), \tag{2.38}$$

where $\bar{\sigma}_{A\gamma}, \bar{\sigma}_{0\gamma}$ and c_γ are material parameters for austenite. From (2.37) and (2.38), the yield stress for austenite phase is given as,

$$\sigma_{Y\gamma} = \bar{\sigma}_{A\gamma} + (\bar{\sigma}_{0\gamma} - \bar{\sigma}_{A\gamma}) \exp(-c_\gamma \vartheta) \qquad [\textit{Yield Stress}] \tag{2.39}$$

Post-yielding, both austenite and martensite phases are known to show power-law hardening behavior (Marshall, 1984; Reed and Horiuchi, 2011) and hence we propose the following phenomenological form for hardening behavior,

$$\bar{\sigma}_\gamma = \bar{\sigma}_{Y\gamma} + K_\gamma \bar{\varepsilon}_{p\gamma}^{q} \qquad [\textit{Hardening Law}] \tag{2.40}$$

where $\bar{\sigma}_\gamma$ is the equivalent tensile stress given in terms of temperature dependent quantities $\bar{\sigma}_{Y\gamma}$, K_γ and q. Similarly for the martensite phase we get,[4]

$$\bar{\sigma}_{\alpha'} = \sigma_{Y\alpha'} + K_{\alpha'} \bar{\varepsilon}_{p\alpha'}^{r} \tag{2.41}$$

where,

$$\sigma_{Y\alpha'} = \bar{\sigma}_{A\alpha'} + (\bar{\sigma}_{0\alpha'} - \bar{\sigma}_{A\alpha'}) \exp(-c_{\alpha'} \vartheta). \tag{2.42}$$

Once the plastic deformation commences, the martensite volume fraction $\phi_{\alpha'}$ evolves with accumulated plastic strain and the yield function for the austenite-martensite composite should account for hardening from the martensite phase as well. We recall Eq. (2.34) to generalize the yield function to austenite-martensite composite,

$$Y(\bar{\varepsilon}_p) = \phi_\gamma \, \bar{\sigma}_\gamma + \phi_{\alpha'} \, \bar{\sigma}_{\alpha'}. \tag{2.43}$$

In the expanded form and after applying (2.33),

$$Y(\bar{\varepsilon}_p) = \phi_\gamma \left\{ \bar{\sigma}_{A\gamma} + (\bar{\sigma}_{0\gamma} - \bar{\sigma}_{A\gamma}) \exp(-c_\gamma \vartheta) + K_\gamma \bar{\varepsilon}_p^{q} \right\} + \phi_{\alpha'} \left\{ \bar{\sigma}_{A\alpha'} + (\bar{\sigma}_{0\alpha'} - \bar{\sigma}_{A\alpha'}) \exp(-c_{\alpha'} \vartheta) + K_{\alpha'} \bar{\varepsilon}_p^{r} \right\}, \tag{2.44}$$

where K_γ, q, $K_{\alpha'}$ and r are temperature-dependent strain hardening parameters. We assume a linear temperature dependence of the following form

$$K_\gamma = K_{\gamma 0} + K_{\gamma 1}(\vartheta - \vartheta_{ref}) \quad \text{and} \quad K_{\alpha'} = K_{\alpha' 0} + K_{\alpha' 1}(\vartheta - \vartheta_{ref}) \tag{2.45}$$

$$q = q_0 + q_1(\vartheta - \vartheta_{ref}) \quad \text{and} \quad r = r_0 + r_1(\vartheta - \vartheta_{ref}). \tag{2.46}$$

In the above we can select a convenient reference temperature and we select it to be the cryogenic temperature such that $\vartheta_{ref} = 77K$.

2.3. Kinetics of phase transformations

The proposed yield function (2.44) in Section 2.2 requires a law for evolution of martensite with plastic strain. We follow the work of Olson and Cohen (1975) who developed a physically-motivated model for the kinetics of austenite-martensite transformation. The transformation process has two main steps: 1) increasing number of shear-band intersection in the untransformed austenite due to the increasing plastic strain, and 2) nucleation of martensitic embryos from the intersection of shear bands. Both these steps are strongly temperature-dependent and stochastic in nature.

Shear-band-free volume is denoted by ϕ_{sb}. As the austenite steel is plastically deformed, the shear-band-free volume in untransformed austenite starts to deplete. The volume fraction of shear bands can then be written as

$$\frac{\dot{\phi}_{sb}}{1 - \phi_{sb}} = \alpha(\vartheta)\dot{\bar{\varepsilon}}_p, \tag{2.47}$$

where α is the temperature-dependent rate of shear-band formation, $\bar{\varepsilon}_p$ is the equivalent plastic strain and $\dot{()}$ denotes derivative with time. α increases with decreasing stacking-fault energy and increasing strain rate, since these factors favor the shear-band deformation mode. The nucleation of martensitic embryos is assumed to occur primarily at the shear-band intersections in a probabilistic manner. The average number of martensitic embryos that form per unit austenite volume, $N_{\alpha'}$ can be given as

$$N_{\alpha'} = pN_I, \tag{2.48}$$

[4] As some of the austenite transforms to martensite, locally there is additional straining in both martensite and austenite phases due to volume expansion in the martensite phase. Our power law mathematical form is an approximation intended to capture the cumulative stress hardening effect in a phenomenological manner.

where N_I denotes the number of shear-band intersections per unit volume and p denotes the probability that an intersection will act as a nucleation site. A power-law dependence of the following form is proposed for the number of shear-band intersections per unit volume

$$N_I = K_g\left(\frac{\phi_{sb}}{v_{sb}}\right)^a, \tag{2.49}$$

where v_{sb} is the average volume of a shear band, K_g is a fixed geometric factor and a is a fixed exponent.

Lastly, the rate of increase of martensite volume fraction, $\dot{\phi}_{\alpha'}$, is given as,

$$\frac{\dot{\phi}_{\alpha'}}{(1-\phi_{\alpha'})} = v_{\alpha'}\dot{N}_{\alpha'} = \beta\dot{\phi}_{sb}^{\ a} \quad \text{where} \quad \beta = \frac{v_{\alpha'}K_g}{(v_{sb})^a}p. \tag{2.50}$$

$v_{\alpha'}$ is the average volume of a martensitic embryo and $(1-\phi_{\alpha'})$ factor indicates decreasing volume available for transformation. (2.47) and (2.50) together describe the temperature-dependent evolution of martensite volume fraction with accumulated plastic strain. For austenitic steels, temperature dependent of $\alpha(\vartheta)$ and $\beta(\vartheta)$ are typically expressed as,

$$\alpha(\vartheta) = \alpha_0 + \alpha_1\vartheta + \alpha_2\vartheta^2 \quad \text{and} \quad \beta(\vartheta) = \beta_0\left\{1 - \text{erf}\left(\frac{\vartheta - \vartheta_0}{\vartheta_1}\right)\right\}, \tag{2.51}$$

where a, α_0, α_1, α_2, β_0, ϑ_0 and ϑ_1 are material parameters and *erf* is error function.

2.4. Material parameters for 316L steel

The elastic properties of 316L steel were taken from Srivastava et al. (2011). Experiments indicate that the shear modulus for steel increases as the temperature decreases from room to cryogenic temperature. We describe this temperature dependence of shear modulus by a linear relationship

$$G(\vartheta) = G_0 - G_1(\vartheta - \vartheta_{ref}). \tag{2.52}$$

Poisson's ratio is taken to be temperature independent and following the assumptions outlined in (2.15), we assume $\nu_\gamma = \nu_{\alpha'} = \nu$.

The parameters a, α_0, α_1, α_2, β_0, ϑ_0 and ϑ_1 for 316L SS were obtained by fitting $\phi_{\alpha'}(\bar{\varepsilon}_p)$ to the experimental data of Spencer et al. (2009) at different temperatures (Fig. 1).

The material parameters for temperature dependence of our proposed yield strength model are found by calibration with data for 316L steel in 77 K to 300 K range (Buitrago et al., 2010; Reed and Horiuchi, 2011; Spencer et al., 2009; Srivastava et al., 2011). As a simplifying assumption, we consider $c_\gamma = c_{\alpha'} = c$. The yield fit is shown in Fig. 2.

The temperature dependence of the flow strength (K_γ and $K_{\alpha'}$) and hardening exponents (q and r) in (2.45) and (2.46) is found by fitting the stress-strain curve to the uniaxial tension test at 77 K and 298 K on flat dog-bone specimens reported in Buitrago et al. (2010); Srivastava et al. (2011).

Note that for martensite, we only have value for $K_{\alpha'}$ and r at reference temperature (77K). We assume that the slope of linear temperature dependence is same for both martensite and austenite. Therefore, as a simplification $K_{\gamma 1} = K_{\alpha' 1} = K_1$, and $q_1 = r_1 = q$ in (2.45) and (2.46). Fig. 3 shows the fit of the model to the tension test data in Srivastava et al. (2011). As shown, the model is able to fit the tension tests at room and cryogenic temperature well. Our proposed model is able to capture the salient feature of strain-induced temperature-dependent austenite to martensite phase transition and corresponding *second strain hardening* at large strains. The summary of all the material parameters for 316L SS is reported in Table 1.

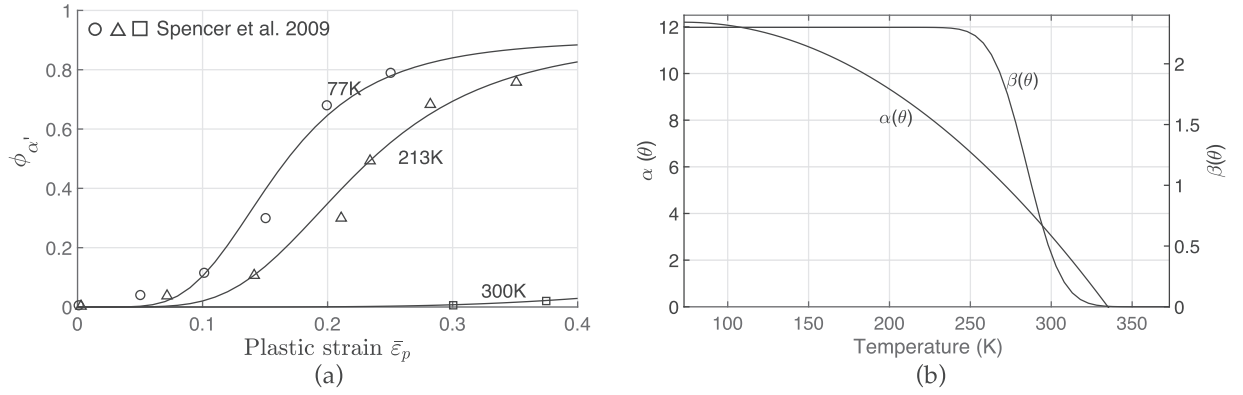

Fig. 1. (a) Evolution of martensite in 316L steel with accumulated plastic strain at 77 K (open circle), 213 K (open triangle) and 300 K (open square). The markers are experimental measurements (Spencer et al., 2009) and solid lines are fit from the model; (b) $\alpha(\vartheta)$ and $\beta(\vartheta)$ as a function of temperature for 316L steel obtained by fitting martensite volume fraction to the data in Spencer et al. (2009).

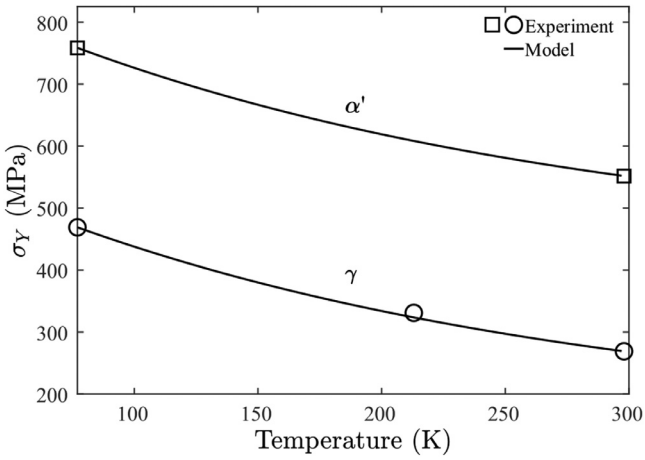

Fig. 2. Yield Strength for 316L steel in cryogenic to room temperature range. Square and circle markers are experimental results (Buitrago et al., 2010; Reed and Horiuchi, 2011; Spencer et al., 2009; Srivastava et al., 2011) and solid line shows our model fit.

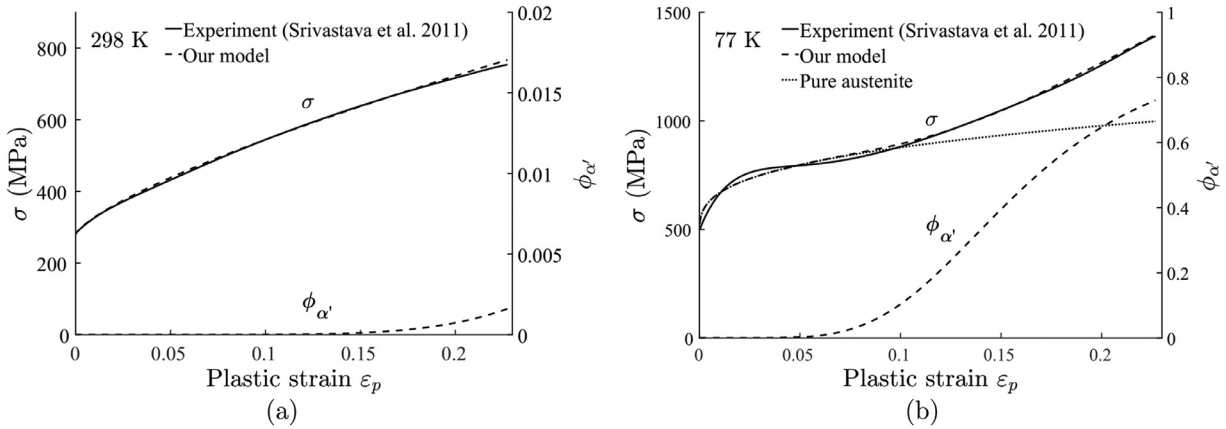

Fig. 3. Model fit for 316L steel uniaxial tensile tests on flat dog-bone specimen at (a) room and (b) cryogenic temperatures. Left-axis: stress-strain curves. Right-axis: martensite evolution prediction by the model.

Table 1
Material parameters for 316L steel.

Parameter	Value	Parameter	Value
G_0	78230 MPa	G_1	66 MPa/K
ν	0.3	ϑ_{ref}	77 K
α_{th}	17.3 $\times 10^{-6}$ 1/K	κ	25.0 W/(m^2 K)
C	0.46 $\times 10^3$ J/(kg K)	l	-1.50×10^4 J/kg
$\bar{\sigma}_{0\gamma}$	597 MPa	$\bar{\sigma}_{0\alpha'}$	884 MPa
$\bar{\sigma}_{A\gamma}$	156 MPa	$\bar{\sigma}_{A\alpha'}$	421 MPa
$K_{\gamma 0}$	827 MPa	$K_{\alpha' 0}$	5330 MPa
K_1	2.74 MPa/K	c	0.0043/K
q_0	0.32	r_0	1.31
q	0.00176/K	a	8.7
α_0	11.25	α_1	0.026/K
α_2	-0.000189/K^2	β_0	1.15
ϑ_0	285 K	ϑ_1	24 K

3. Representative thermo-mechanical histories

We implemented our 3D model in the commercial software Abaqus/Standard by writing a user material subroutine (UMAT) and developed a numerical simulation capability to model and simulate thermo-mechanical loading history of 316L steel. In this section, we discuss results for three representative thermo-mechanical history cases considering uniaxial and quasi-static loading conditions.

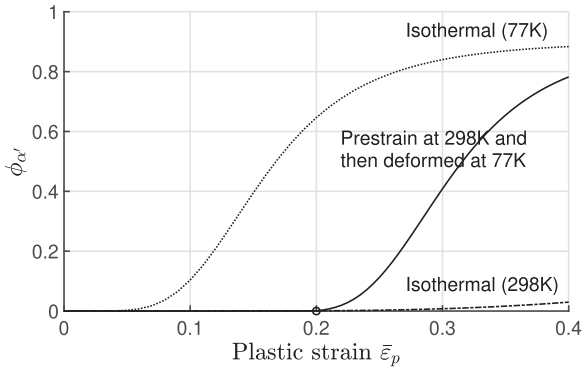

Fig. 4. Evolution of volume fraction of martensite with change in temperature at $\bar{\varepsilon}^*$ (indicated by the black circle mark).

3.1. Martensite evolution for consecutive deformations at two different temperatures

Olson and Cohen (1975) considered only isothermal deformations in their study. Following their seminal work and our framework, we consider a deformation example to illustrate the evolution of volume fraction of martensite in a virgin austenitic steel that undergoes the following sequence of events: i) deformed up to an equivalent plastic strain $\bar{\varepsilon}_p = \bar{\varepsilon}^*$ at temperature ϑ_s, ii) unloaded (reduce force to zero) while maintaining the temperature ϑ_s, iii) let the temperature drop from ϑ_s to ϑ_f ($\vartheta_f < \vartheta_s$) without deformation constraint, and iv) deformed the unloaded material at ϑ_f.

The shear-band volume fraction evolves according to (2.50). The rate of evolution is governed by the temperature-dependent parameter α. For the following loading scenario,

$$\vartheta = \begin{cases} \vartheta_s & \bar{\varepsilon}_p \le \bar{\varepsilon}^* \\ \vartheta_f & \bar{\varepsilon}_p > \bar{\varepsilon}^* \end{cases} \tag{3.1}$$

the coupled equations for shear-band and martensite volume-fraction evolution with $\bar{\varepsilon}_p$ are given as,

$$\dot{\phi}_{sb} = \begin{cases} (1-\phi_{sb})\alpha_s \dot{\bar{\varepsilon}}_p & \bar{\varepsilon}_p \le \bar{\varepsilon}^* \\ (1-\phi_{sb})\alpha_f \dot{\bar{\varepsilon}}_p & \bar{\varepsilon}_p > \bar{\varepsilon}^* \end{cases} \quad \text{and} \quad \phi_{sb}(\bar{\varepsilon}_p = 0) = 0 \tag{3.2}$$

$$\dot{\phi}_{\alpha'} = \begin{cases} (1-\phi_{\alpha'})\beta_s \dot{\phi}_{sb}{}^a & \bar{\varepsilon}_p \le \bar{\varepsilon}^* \\ (1-\phi_{\alpha'})\beta_f \dot{\phi}_{sb}{}^a & \bar{\varepsilon}_p > \bar{\varepsilon}^* \end{cases} \quad \text{and} \quad \phi_{\alpha'}(\bar{\varepsilon}_p = 0) = 0 \tag{3.3}$$

where,

$$\alpha(\vartheta_s) \equiv \alpha_s \quad \text{and} \quad \alpha(\vartheta_f) \equiv \alpha_f. \tag{3.4}$$

$$\beta(\vartheta_s) \equiv \beta_s \quad \text{and} \quad \beta(\vartheta_f) \equiv \beta_f. \tag{3.5}$$

Fig. 4 shows the evolution of martensite volume fraction with change in temperature[5] from $\vartheta_s = 298$ K to $\vartheta_f = 77$ K using the reported material model parameters in Table 1 for 316L steel.

After straining and then unloading at 298 K, when the temperature changes from 298 K to 77 K under constraint-free condition, the martensite volume fraction remains unchanged during temperature drop. When the material is subsequently deformed at 77 K, the martensite volume fraction begins to evolve, albeit at a different rate. The rate of martensite evolution is higher at 77 K (indicated by the circular mark). The resulting martensite content thus lies between the two isothermal curves at 77 K and 298 K.

3.2. Work-hardened to 10% strain at 298 K followed by deformation at various cryogenic temperatures

In the first step, virgin 316L steel is strained to 10% and unloaded to account for typical room temperature forming. This is followed by deformation at different cryogenic temperatures which represent application of room temperature formed 316L steel subjected to operating loads at cryogenic temperatures. Usingour model, we study how the material response varies under different cryogenic temperatures. Pre-straining 316L steel at room temperature induces a negligible volume fraction of martensite as is evident from Fig. 1. When this sample is loaded again at cryogenic temperature, the initial response is

[5] In the integrated from, Eqs. 3.2 and 3.3 give the following expression for martensite volume-fraction

$$\phi_{\alpha'} = \begin{cases} 1-\exp\{-\beta_s[1-\exp(-\alpha_s\bar{\varepsilon}_p)]^a\} & \bar{\varepsilon}_p \le \bar{\varepsilon}^* \\ 1-\exp\{-(\beta_s-\beta_f)[1-\exp(-\alpha_s\bar{\varepsilon}^*)]^a\}\exp\{-\beta_f[1-\exp(-(\alpha_s-\alpha_f)\bar{\varepsilon}^*-\alpha_f\bar{\varepsilon}_p)]^a\} & \bar{\varepsilon}_p > \bar{\varepsilon}^* \end{cases}$$

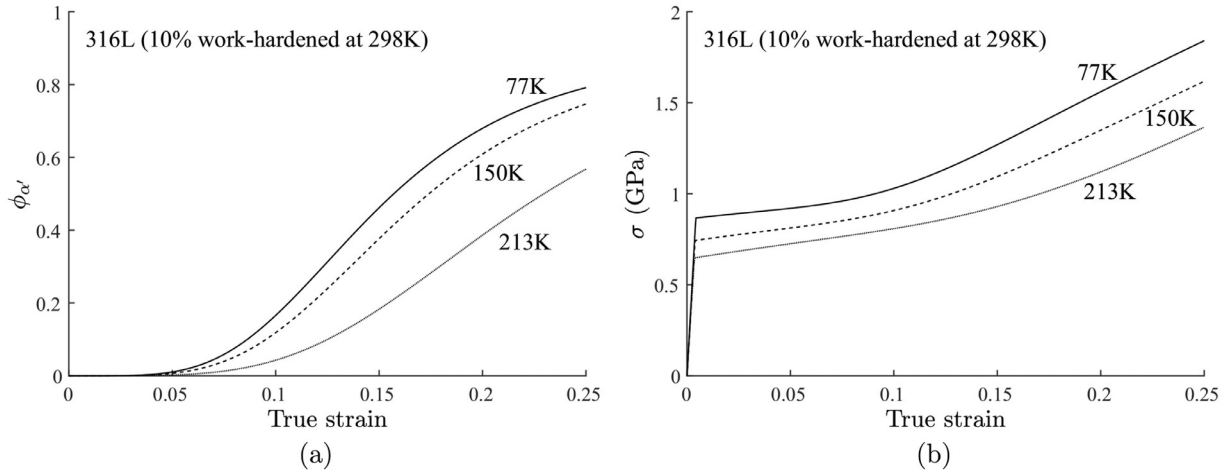

Fig. 5. Model prediction of (a) martensite volume fraction-strain responses and (b) stress-strain responses for 316L steel pre-strained (work hardened) to 10% strain and unloaded at room temperature (298K) and then deformed at cryogenic 77K, 150K, and 213K.

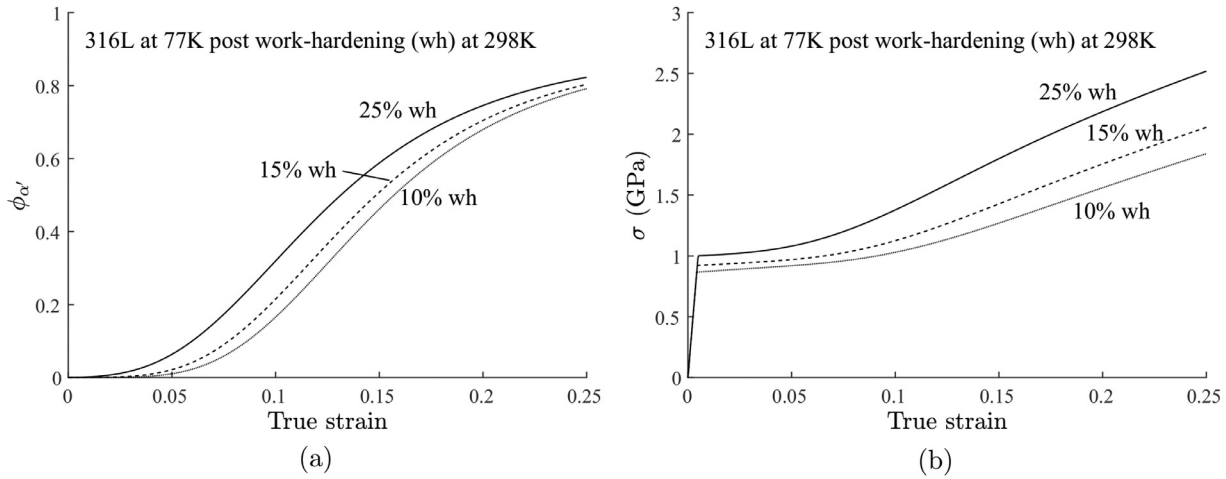

Fig. 6. Model prediction of (a) martensite volume fraction-strain responses and (b) stress-strain responses for 316L steel work-hardened to three different strains 10%, 15%, and 25% and then unloaded at room temperature (298K) - then deformed further at 77 K.

elastic. Lower the temperature, the higher the initial yield, higher the rate of martensite formation and higher the strain hardening, thus resulting in higher stresses at lower temperature deformations as shown in Fig. 5.

3.3. Work-hardened to varying strains at 298 K followed by deformation at 77 K

In the first step, 316L steel is work-hardened at 298 K by uniaxially deforming it to three different strain cases of 10%, 15% and 25% and then unloading it. The work-hardened 316L is then subsequently deformed at 77 K. While a higher work-hardening at 298 K does not lead to any appreciable martensite volume fraction, it produces higher shear-band volume fraction. A higher shear-band volume fraction provides a higher probability of intersection of shear-bands and potential nucleation sites for martensitic embryos as the temperature is lowered. Thus higher degree of work-hardening at room temperature leads to a higher volume fraction of martensite at cryogenic temperatures which then leads to larger stresses as it is predicted by the model and shown in Fig. 6.

4. Model validation using full scale experiments

We applied our model and 3D numerical simulation capability using a UMAT implementation in Abaqus, and carried out simulations[6] involving inhomogeneous deformation of a full-scale 316L steel corrugated pipe (C-pipe) for which experimental results were published in Buitrago et al. (2010); Srivastava et al. (2011). Note quasi static/slow deformation

[6] The full-scale C-pipes used in the experiments were made of same 316L SS for which we have calibrated our material parameters. Previously calibrated model parameters in Table 1 using simple flat-sheet coupon tests were not changed for the validation simulations.

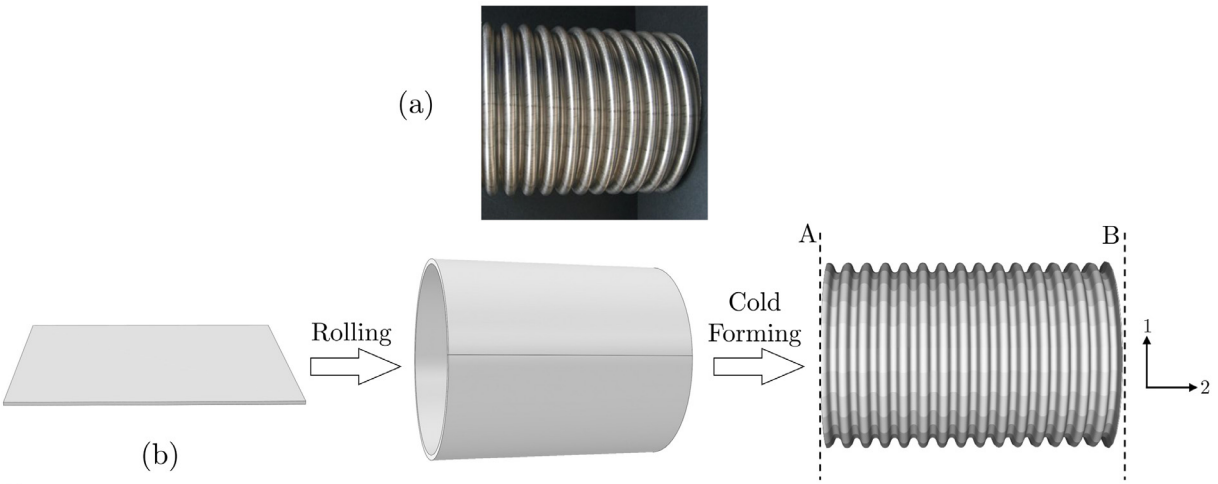

Fig. 7. (a) A section of a real *helical* C-pipe. (b) Schematic of full scale manufacturing of a corrugated pipe. All the steps are accounted for in our finite element analysis.

in the experiments allow any heat generated inside the material due to plastic work and phase transformation to dissipate to the ambient without causing material temperature rise. Fig. 7(a) shows a segment of the C-pipe used in the compression and tension tests. The C-pipes are formed at room temperature and are used as *flexible LNG transfer pipes* which are subjected to severe operational loads at cryogenic temperatures.

The numerical simulations were carried out for *force-versus-global strain* response of the 316L steel corrugated pipe (C-pipe) which was subjected to following thermo-mechanical forming history: at room temperature (298K), an initially flat sheet was mechanically rolled and seam-welded into a cylinder pipe. Then helical corrugations were cold formed at room temperature with an external die that revolved around the pipe which was being pulled in the axial direction. This corrugation formation process is illustrated in Fig. 7(b). The *global pipe axial strain* is defined as the change in pipe length divided by the initial pipe length. Tension and compression test were done on the corrugated pipes at both room temperature (298 K) and cryogenic temperature (77 K). In the experiments, 10-pitch long pipe segments were used. Nominal dimensions for the outer diameter, inner diameter and the thickness of the pipes were 298 mm, 264 mm and 1.3 mm, respectively. The sinusoidal shaped corrugation had an amplitude of 7.8 mm and a pitch length 30.2 mm.

Finite element simulations were conducted using Abaqus CAX4 element and replicated the complete thermo-mechanical history of the pipe making followed by the compression and tension test conditions.[7] Our finite element simulation consisted of following three steps:

(i) *Rolling*: Rolling of flat sheet into a cylindrical form was not explicitly performed in our finite element simulations. Effective residual strain from roll forming was estimated[8] and added to the starting axisymmetric geometry representing a cylindrical pipe, as initial residual strain prior to subsequent finite element simulation steps.
(ii) *Corrugation forming*: Room temperature corrugation forming operation was simulated by applying a sinusoidal concentrated nodal load profile along 1-direction to deform the initially straight pipe. The force profile and nodal force magnitudes were calibrated to form the corrugation geometry to match the geometry in Srivastava et al. (2011).
(iii) *Corrugated pipe deformation*: Following the C-pipe forming steps, uniaxial tension and compression simulations at both room and cryogenic temperatures were conducted. Analysis was performed by fixing 2-direction displacement of one of the sides (side A) and applying 2-direction (axial) displacement to the other side (side B).

Fig. 8 (a) and (b) show the experimental and finite element simulation of force-versus-global strain results for tension and compression tests, respectively, at room and cryogenic temperatures. The pipe is stiffer at 77 K as the uniaxial tests demonstrated in Fig. 3 and accordingly requires larger forces to deform it as compared to deforming it at 298 K. In the tension test, at large strains, the corrugations on the pipe are stretched flat to a point where material elongation takes over geometric elongation, leading to a rapid hardening response. On the other hand, in the compression test, with increasing compressive strain, the corrugations start to collapse as indicated by the nearly flat region of the curve. Comparisons between the simulation prediction and experimental results show good predictive capability of the model[9]

[7] Srivastava et al. showed that there were no distinguishable mechanical response differences between helical corrugations and axisymmetric corrugation geometry. Therefore for numerical simulation efficiency, we have used axisymmetric geometry assumption.

[8] Maximum residual strain from rolling was found to be < 0.005.

[9] Note the results are strongly dependent on pipe forming history as it was shown and discussed in Srivastava et al. (2011). In Srivastava et al. (2011), a very simplified model was applied to show the strong effect of forming history but this model did not account for the austenite to martensite transformation that occurs at cryogenic temperature.

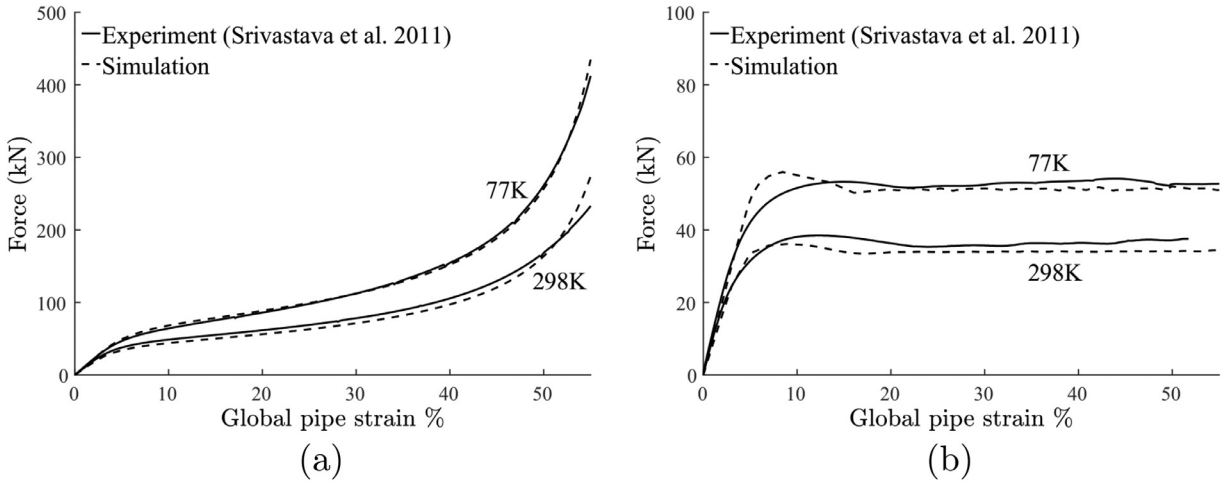

Fig. 8. Force *versus* global pipe strain of a room temperature preformed C-pipe under (a) tensile load and (b) compressive load. Simulation results (dotted lines) are plotted against experiments (solid lines) for room and cryogenic temperature.

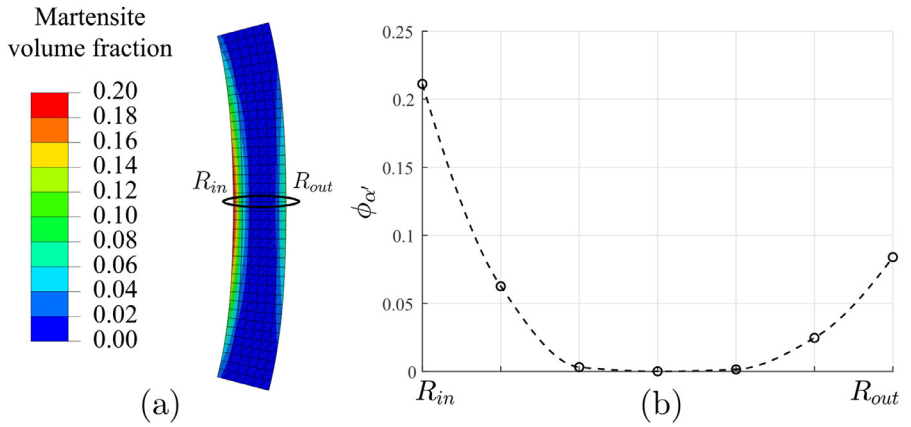

Fig. 9. C-pipe outer bend thickness cross-section at 40% global tensile strain at cryogenic temperature. (a) Martensite volume fraction contours in the pipe corrugation thickness. (b) Martensite volume fraction in the radial direction across the pipe corrugation thickness.

After validating the predictive capability of the model, we used simulations to examine the local martensite formation in the corrugated pipe. Fig. 9 shows martensite distribution in the C-pipe's outer bend for 40% global C-pipe tensile strain at 77 K. The results show that higher volume fraction of martensite is formed at the inner and outer surfaces of the pipe corrugation due to higher local strains at the inner and outer surfaces. Fig. 9(a) and (b) further show that the simulation predicts higher content of martensite near the inner surface as compared to the outer surface. During the initial corrugation forming, near the outer bend of the corrugation, the inner surface accumulates compressive strains while the outer surface accumulates tensile strains (this effect is reversed near the inner bend). Following the corrugation forming, when the C-pipe is stretched to a high global tensile strain, the corrugations open to become nearly flat and both the inner and the outer corrugation surfaces approach same tensile strain state. This results in regions that were subjected to compressive strains during corrugation forming, experiencing higher net accumulated plastic strains and resulting in higher martensite formation in these regions.

5. Simulation predictions for a notched flat plate

Understanding the local and global effects of geometric imperfections such as notches on the material is critical for a variety of engineering applications. Notches are critical as the stress and strain concentration near the notch tip can lead to crack initiation and fracture, therefore flat plate notch tests are commonly conducted when structural damage assessment is of concern (Oh et al., 2007; 2011; Tanguy et al., 2008).

Notch effects in metastable austenitic steel structures are strongly temperature dependent and especially complex at cryogenic temperatures due to the coupled thermo-mechanical and austenite-martensite phase transformation. We use our model and finite element simulation capability to evaluate notch effects using a representative 316L steel plate at room and cryogenic temperatures.

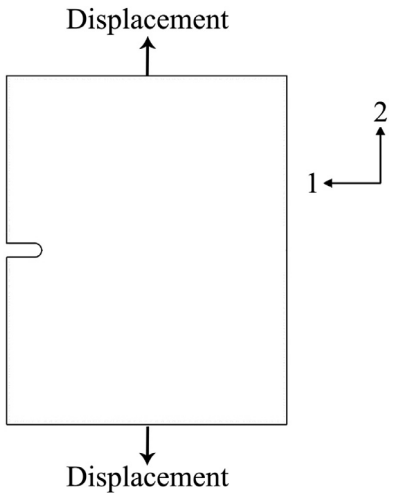

Fig. 10. Schematic of a notched flat plate with tensile loading boundary conditions.

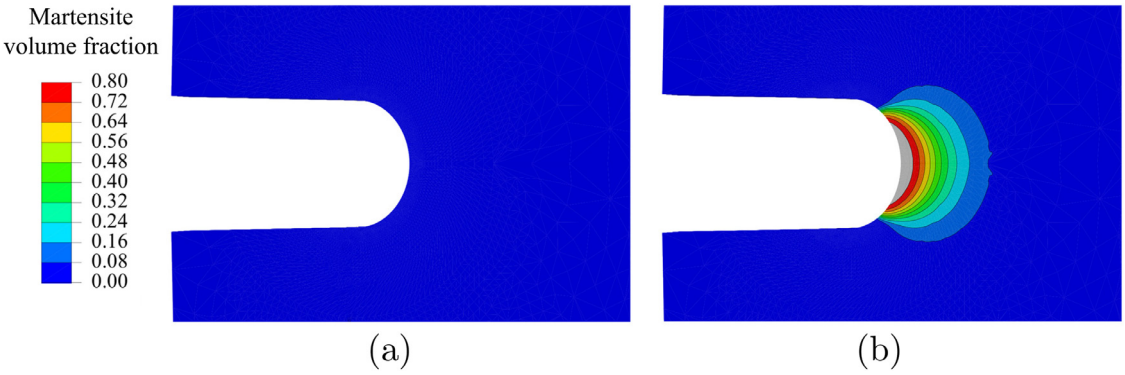

Fig. 11. Simulation prediction of martensite volume fraction near the notch tip for 2% global plate strain at (a) room temperature, and (b) cryogenic temperature. The contour is plotted for a cross-section at the middle of the plate thickness. Grey color indicates values greater than maximum in the legend scale.

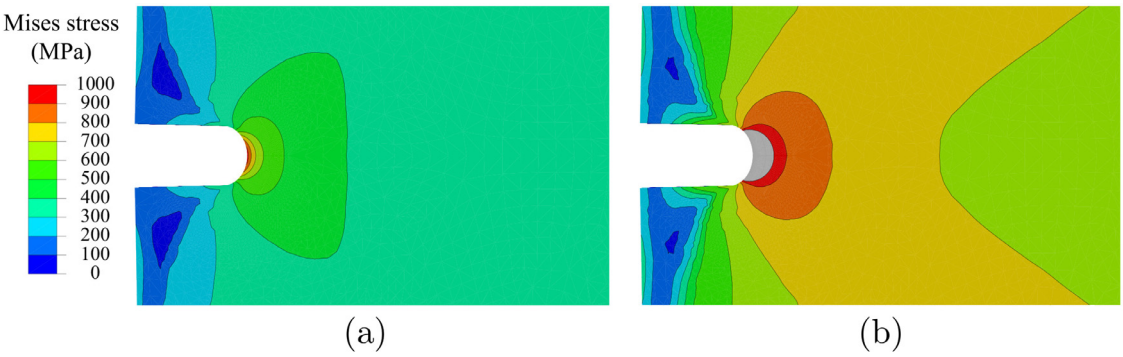

Fig. 12. Simulation prediction of Mises stress for 2% global plate strain at (a) room temperature, and (b) cryogenic temperature. The contour is plotted for a cross-section at the middle of the thickness. Grey color indicates values greater than maximum in the legend scale.

A 50 mm X 40 mm plate with 5 mm thickness was analysed in the simulation (Fig. 10 shows the schematic). The notch length was 5 mm and the notch tip radius was 1 mm. Material parameters for 316L shown in Table 1 were used for simulation. A displacement boundary condition was applied in 2-direction to stretch the notched plate. Abaqus C3D8 element was utilized in the simulations, along with the implemented UMAT. All simulations results are shown for the through-thickness mid-plane of the plate. Comparison of martensite volume fraction near the notch tip for the room and cryogenic temperatures at 2% global far-field tensile strain is shown in Fig. 11. For the same applied far-field strain, notched plate at cryogenic temperature shows significantly larger martensite volume fraction than a plate strained at room temperature. The

simulation can predict quantitative values of martensite formation and the results show that the phase transition is localized near the notch tip where the equivalent plastic strain possess largest values.

A comparison of Mises stress for the room and cryogenic temperature deformation cases shown in Fig. 12, clearly indicates a strong influence of temperature dependent phase transformation on distribution and magnitude of stress field along the notched flat plate. Safe design and application of metastable material structures at cryogenic temperatures will require an accurate prediction of local and global stresses and austenite-martensite material phases. As demonstrated, the model proposed in this paper is able to provide material and mechanical response reasonably well.

6. Concluding remarks

We have developed a thermo-mechanically coupled constitutive theory and a numerical simulation capability for modeling the response of phase transitioning austenitic steels in ambient to cryogenic temperature range. The model parameters were calibrated for 316L stainless steel using tension test data at room and cryogenic temperatures. Our validation study on full-scale 316L stainless steel corrugated pipe illustrates that the model is in good agreement with experimental results. Our proposed constitutive theory is able to model the effects of complex thermo-mechanical histories experienced due to forming and application occurring at different temperatures. We envision that such models can be useful for guiding safe design of austenitic steel based cryogenic and low temperature structures.

Declaration of Competing Interest

None.

Acknowledgements

The authors would like to thank Brown University's School of Engineering for supporting this research.

References

Angel, T., 1954. Formation of martensite in austenitic stainless steels. J. Iron Steel Inst. 177, 165–174.
Bleck, W., Schael, I., 2000. Determination of crash-relevant material parameters by dynamic tensile tests. Steel Res. 71 (5), 173–178. doi:10.1002/srin.200005709.
Brown, S.B., Kim, K.H., Anand, L., 1989. An internal variable constitutive model for hot working of metals. Int. J. Plast. 5 (2), 95–130. doi:10.1016/0749-6419(89)90025-9.
Buitrago, J., Slocum, S.T., Hudak, S.J., Long, R., 2010. Cryogenic structural performance of corrugated pipe. In: Proceedings of the ASME 2010 29th International Conference on Ocean, Offshore and Arctic Engineering: Volume 6. American Society of Mechanical Engineers, pp. 331–342.
Celada-Casero, C., Kooiker, H., Groen, M., Post, J., San-Martin, D., 2017. In-situ investigation of strain-induced martensitic transformation kinetics in an austenitic stainless steel by inductive measurements. Metals (Basel) 7 (7). doi:10.3390/met7070271.
Choi, J.K., Lee, S.-G., Park, Y.-H., Han, I.-W., Morris, J. J., 2012a. High Manganese Austenitic Steel For Cryogenic Applications.
Choi, S.W., Roh, J.U., Kim, M.S., Lee, W.I., 2012. Analysis of two main LNG CCS (cargo containment system) insulation boxes for leakage safety using experimentally defined thermal properties. Appl. Ocean Res. 37, 72–89. doi:10.1016/J.APOR.2012.04.002.
Chul Kim, B., Ho Yoon, S., Gil Lee, D., 2011. Pressure resistance of the corrugated stainless steel membranes of LNG carriers. Ocean Eng. 38 (4), 592–608. doi:10.1016/J.OCEANENG.2010.12.013.
Conrad, H., 1964. Thermally activated deformation of metals. J. Metals 16 (7), 582–588.
Conrad, H., 1970. The athermal component of the flow stress in crystalline solids. Mater. Sci. Eng. 6 (4), 265–273.
Conrad, H., Wiedersich, H., 1960. Activation energy for deformation of metals at low temperatures. Acta Metall. 8 (2), 128–130.
Diani, J., Parks, D., 1998. Effects of strain state on the kinetics of strain-induced martensite in steels. J. Mech. Phys. Solids 46 (9), 1613–1635.
Garion, C., Skoczen, B., 2002. Modeling of plastic strain-induced martensitic transformation for cryogenic applications. J. Appl. Mech. 69 (6), 755–762.
Garion, C., Skoczeń, B., Sgobba, S., 2006. Constitutive modelling and identification of parameters of the plastic strain-induced martensitic transformation in 316l stainless steel at cryogenic temperatures. Int. J. Plast. 22 (7), 1234–1264. doi:10.1016/J.IJPLAS.2005.08.002.
Gavriljuk, V., Theisen, W., Sirosh, V., Polshin, E., Kortmann, A., Mogilny, G., Petrov, Y.N., Tarusin, Y.V., 2013. Low-temperature martensitic transformation in tool steels in relation to their deep cryogenic treatment. Acta Mater. 61 (5), 1705–1715. doi:10.1016/j.actamat.2012.11.045.
Hamasaki, H., Ohno, T., Nakano, T., Ishimaru, E., 2018. Modelling of cyclic plasticity and martensitic transformation for type 304 austenitic stainless steel. Int. J. Mech. Sci. 146–147, 536–543. doi:10.1016/j.ijmecsci.2017.12.003.
Iwamoto, T., 2004. Multiscale computational simulation of deformation behavior of TRIP steel with growth of martensitic particles in unit cell by asymptotic homogenization method. Int. J. Plast. doi:10.1016/j.ijplas.2003.05.002.
Jacques, P., Furnémont, Q., Lani, F., Pardoen, T., Delannay, F., 2007. Multiscale mechanics of TRIP-assisted multiphase steels: i. characterization and mechanical testing. Acta Mater. 55 (11), 3681–3693. doi:10.1016/J.ACTAMAT.2007.02.029.
Kim, J.-H., Kim, S.-K., Kim, M.-S., Lee, J.-M., 2014. Numerical simulation of membrane of LNG insulation system using user defined material subroutine. J. Comput. Struct. Eng.Inst. Kor. 27 (4), 265–271. doi:10.7734/COSEIK.2014.27.4.265.
Kim, J.-J.J.-H., Park, W.-S., Chun, M.-S., Kim, J.-J.J.-H., Bae, J.-H., Kim, M.-H., Lee, J.-M., 2012. Effect of pre-straining on low-temperature mechanical behavior of AISI 304l 543, 50–57.
Kim, S.-K., Lee, C.-S., Kim, J.-H., Kim, M.-H., Lee, J.-M., 2013. Computational evaluation of resistance of fracture capacity for SUS304l of liquefied natural gas insulation system under cryogenic temperatures using ABAQUS user-defined material subroutine. Mater. Des. 50, 522–532. doi:10.1016/J.MATDES.2013.03.064.
Kim, Y.H., Kim, K.Y., Lee, Y.D., 2004. Nitrogen-alloyed, metastable austenitic stainless steel for automotive structural applications. Mater. Manuf. Process. 19 (1), 51–59. doi:10.1081/AMP-120027498.
Kocks, U., Mecking, H., 2003. Physics and phenomenology of strain hardening: the fcc case. Progress Mater. Sci. 48, 171–273.
Koistinen, D., Marburger, R., 1959. A general equation prescribing the extent of the austenite-martensite transformation in pure iron-carbon alloys and plain carbon steels. Acta Metall. 7 (1), 59–60. doi:10.1016/0001-6160(59)90170-1.
Lee, E., 1969. Elastic-plastic deformations at finite strains. J. Appl. Mech. 36, 1–6.
Lee, K.J., Chun, M.S., Kim, M.H., Lee, J.M., 2009. A new constitutive model of austenitic stainless steel for cryogenic applications. Comput. Mater. Sci. 46 (4), 1152–1162. doi:10.1016/J.COMMATSCI.2009.06.003.

Lee, T.-H., Kim, S.-D., Ha, H.-Y., Jang, J.H., Moon, J., Kang, J.-Y., Lee, C.-H., Park, S.-J., Woo, W., Shin, J.-H., Lee, J.-W., Suh, D.-W., Hong, H.-U., 2019. Screw dislocation driven martensitic nucleation: a step toward consilience of deformation scenario in fcc materials. Acta Mater. 174, 342–350. doi:10.1016/j.actamat.2019.05.050.

Lee, Y.-S., Ishikawa, K., Okayasu, M., 2019. Influence of strain induced martensite formation of austenitic stainless steel on wear properties. Met. Mater. Int. 25 (3), 705–712. doi:10.1007/s12540-018-00229-4.

Levitas, V., Idesman, A., Olson, G., 1998. Continuum modeling of strain-induced martensitic transformation at shear-band intersections. Acta Mater. 47 (1), 219–233. doi:10.1016/S1359-6454(98)00314-0.

Levitas, V.I., 1997. Phase transitions in elastoplastic materials: continuum thermomechanical theory and examples of control. part ii. J. Mech. Phys. Solids 45 (7), 1203–1222.

Levitas, V.I., 1997. Phase transitions in elastoplastic materials: continuum thermomechanical theory and examples of control—part i. J. Mech. Phys. Solids 45 (6), 923–947.

Levitas, V.I., 1998. Thermomechanical theory of martensitic phase transformations in inelastic materials. Int. J. Solids Struct. 35 (9–10), 889–940. doi:10.1016/S0020-7683(97)00089-9.

Mansourinejad, M., Ketabchi, M., 2017. Modification of Olson–Cohen model for predicting stress-state dependency of martensitic transformation. Mater. Sci. Technol. 33 (16), 1948–1954. doi:10.1080/02670836.2017.1342016.

Marshall, P., 1984. Austenitic stainless steels: Microstructure and mechanical properties. Elsevier Science Publishing Co., Inc.

Narutani, T., Olson, G.B., Cohen, M., 1982. Constitutive flow relations for austenitic steels during strain induced martensitic transformation. Le J. de Physique Colloques doi:10.1051/jphyscol:1982465.

Oh, C.-K., Kim, Y.-J., Baek, J.-H., Kim, Y.-P., Kim, W., 2007. A phenomenological model of ductile fracture for api x65 steel. Int. J. Mech. Sci. 49 (12), 1399–1412. doi:10.1016/j.ijmecsci.2007.03.008.

Oh, C.-S., Kim, N.-H., Kim, Y.-J., Baek, J.-H., Kim, Y.-P., Kim, W.-S., 2011. A finite element ductile failure simulation method using stress-modified fracture strain model. Eng. Fract. Mech. 78 (1), 124–137. doi:10.1016/j.engfracmech.2010.10.004.

Olson, G.B., Cohen, M., 1975. Kinetics of strain-induced martensitic nucleation. Metall. Trans. A 6 (4), 791–795. doi:10.1007/BF02672301.

Reed, R.P., Horiuchi, T., 2011. Austenitic steels at low temperatures. Springer US doi:10.1007/978-1-4613-3730-0.

Ryoo, D.-Y., Kang, N., Kang, C.-Y., 2011. Effect of ni content on the tensile properties and strain-induced martensite transformation for 304 stainless steel. Mater. Sci. Eng. A 528 (6), 2277–2281. doi:10.1016/J.MSEA.2010.12.022.

Seeger, A., 1955. CXXXII. The generation of lattice defects by moving dislocations, and its application to the temperature dependence of the flow-stress of f.c.c. crystals. The London, Edinburgh, and Dublin Philosophic.Mag. J. Sci. 46 (382), 1194–1217. doi:10.1080/14786441108520632.

Spencer, K., Véron, M., Yu-Zhang, K., Embury, J.D., 2009. The strain induced martensite transformation in austenitic stainless steels: part 1—Influence of temperature and strain history. Mater. Sci. Technol. 25 (1), 7–17. doi:10.1179/174328408X293603.

Srivastava, V., Buitrago, J., Slocum, S.T., 2011. Stress analysis of a cryogenic corrugated pipe. In: Proceedings of the ASME 2011 30th International Conference on Ocean, Offshore and Arctic Engineering: Volume 3. American Society of Mechanical Engineers, pp. 411–422.

Srivastava, V., Chester, S.A., Ames, N.M., Anand, L., 2010. A thermo-mechanically-coupled large-deformation theory for amorphous polymers in a temperature range which spans their glass transition. Int. J. Plast. 26 (8), 1138–1182.

Srivastava, V., Chester, S.A., Anand, L., 2010. Thermally actuated shape-memory polymers: experiments, theory, and numerical simulations. J. Mech. Phys. Solids 58 (8), 1100–1124.

Stringfellow, R., Parks, D., Olson, G., 1992. A constitutive model for transformation plasticity accompanying strain-induced martensitic transformations in metastable austenitic steels. Acta Metall. Mater. 40 (7), 1703–1716. doi:10.1016/0956-7151(92)90114-T.

Talonen, J., Hanninen, H., 2007. Formation of shear bands and strain-induced martensite during plastic deformation of metastable austenitic stainless steels. Acta Mater. 15 (18), 6108–6118. doi:10.1016/j.actamat.2007.07.015.

Tanguy, B., Luu, T., Perrin, G., Pineau, A., Besson, J., 2008. Plastic and damage behaviour of a high strength x100 pipeline steel: experiments and modelling. Int. J. Press. Vessels Pip. 85 (5), 322–335. doi:10.1016/j.ijpvp.2007.11.001.

Tomita, Y., Iwamoto, T., 1995. Constitutive modeling of trip steel and its application to the improvement of mechanical properties. Int. J. Mech. Sci. 37 (12), 1295–1305. doi:10.1016/0020-7403(95)00039-Z.

Tyshchenko, A., Theisen, W., Oppenkowski, A., Siebert, S., Razumov, O., Skoblik, A., Sirosh, V., Petrov, Y.N., Gavriljuk, V., 2010. Low-temperature martensitic transformation and deep cryogenic treatment of a tool steel. Mater. Sci. Eng. A 527 (26), 7027–7039.

Wang, Z., Beese, A.M., 2019. Stress state-dependent mechanics of additively manufactured 304l stainless steel: part 1—characterization and modeling of the effect of stress state and texture on microstructural evolution. Mater. Sci. Eng. A 743, 811–823. doi:10.1016/j.msea.2018.11.094.

Yang, Z., Yan, J., Chen, J., Lu, Q., Yue, Q., 2017. Multi-objective shape optimization design for liquefied natural gas cryogenic helical corrugated steel pipe. J. Offshore Mech. Arct. Eng. 139 (5), 051703.

Zaera, R., Rodríguez-Martínez, J., Casado, A., Fernández-Sáez, J., Rusinek, A., Pesci, R., 2012. A constitutive model for analyzing martensite formation in austenitic steels deforming at high strain rates. Int. J. Plast. 29, 77–101. doi:10.1016/j.ijplas.2011.08.003.

Zecevic, M., Upadhyay, M.V., Polatidis, E., Panzner, T., Swygenhoven, H.V., Knezevic, M., 2019. A crystallographic extension to the olson-cohen model for predicting strain path dependence of martensitic transformation. Acta Mater. 166, 386–401. doi:10.1016/j.actamat.2018.12.060.